MATERIALS CHEMISTRY
FRONTIERS

RESEARCH ARTICLE

View Article Online
View Journal | View Issue

Cite this: *Mater. Chem. Front.*, 2023, 7, 4080

Received 10th May 2023,
Accepted 19th June 2023

DOI: 10.1039/d3qm00537b

rsc.li/frontiers-materials

# Engineering the intermediate adduct phase to control the crystallization of perovskites for efficient and stable perovskite solar cells†

Muhammad Mateen,‡[a] Ziyu Li,‡[a] Hongxi Shi,[a] Hao Huang,[a] Danish Khan,[b] Raja Azhar Ashraaf Khan,[a] Muhammad Rafiq,[c] Jawad Ali Shah Syed,[d] Afshan Khaliq,[a] Ghulam Abbas Ashraf,[a] Jadel Matondo Tsiba,[e] Zhangbo Lu,[a] Dan Chi*[a] and Shihua Huang*[a]

Perovskite solar cells (PSCs), on account of their ever-increasing power conversion efficiency (PCE), are captivating industrialists. Despite this, the performance of perovskite solar cells, especially the long life span, is the main barrier to PSCs' commercial deployment where the inefficient perovskite layer is always convicted as the key reason behind it. In reality, the perovskite layer suffers from different intermediate transformations where dimethyl sulfoxide (DMSO), forming $PbI_2$·DMSO intermediates, plays an essential role in retarding the rapid crystallization of perovskite. Therefore, these intermediate phases govern the morphologies and crystallinities of the final perovskite films. In the comparison of $FAPbI_3$ and $MAPbI_3$, which are the two most studied single-cation perovskites, during intermediate phase conversions, the $PbI_2$·MAI·DMSO adduct provides high-quality perovskite than the $PbI_2$·FAI·DMSO adduct, which leads to the poor film quality of FA-based single cation and mixed cation perovskites. Herein, the intermolecular exchange of DMSO with FAI in the $PbI_2$·MAI·DMSO adduct is performed to get $MA_xFA_{1-x}PbI_3$ films where the grain size is dramatically enhanced, and a PCE of 20.79% is obtained with superior long term stability.

## Introduction

Due to the unprecedented escalation in the power conversion efficiency (PCE) of perovskite solar cells (PSCs), the photovoltaic (PV) industry is considering replacing not only thin film PV but also conventional silicon PV with PSC modules. Following this line of thought, the fabrication methods of the perovskite layer should be scaled up where crystal adjustment and compositional engineering play a big part.[1,2] $MAPbI_3$ and $FAPbI_3$ are two basic perovskites on which most of the research is being carried out. Although the stability of $FAPbI_3$ is much better than that of $MAPbI_3$, the conversion of the photo-inactive δ-phase to the photoactive α-phase increases the complications in fabrication methods.[3–5] As a result, the mixed cation perovskites are preferred over that with a single cation (MA or FA) to avoid the issues of phase conversion and instability.[6–8]

Among two widely employed methods, including the one-step anti-solvent method and two-step deposition, the two-step method improves the perovskite morphological properties such as high crystallinity and large grain sizes.[8–15] Still, the control of perovskite composition is a strenuous task.[16] The one-step anti-solvent method is generally preferred over the two-step method to enhance the performance of PSCs, but it results in a small grain size.[17–20] As a consequence, a huge ratio of grain boundaries and defects is generated in perovskites. To cure these defects, different strenuous strategies are applied in the form of passivation layers and hole transport material (HTM) modifications.[18–21] Instead of these complications, modifying compositional engineering to develop the perovskite layer with improved grain sizes and fewer defects through a one step anti-solvent procedure is a productive avenue. Generally, in $MAPbI_3$-based perovskite precursors, an adduct of $PbI_2$·MAI·DMSO is

---

[a] *Provincial Key Laboratory of Solid-State Optoelectronic Devices, Zhejiang Normal University, Jinhua 321004, China. E-mail: chidan@zjnu.edu.cn, huangshihua@zjnu.cn*
[b] *College of New Materials and New Energies, Shenzhen Technology University, Shenzhen 518118, Guangdong, China*
[c] *Institute of Biomedical Materials and Engineering, College of Materials Science and Engineering, Qingdao University, Qingdao, 266071, China*
[d] *National Laboratory of Solid-State Microstructure, Materials Science & Engineering Department, College of Engineering and Applied Sciences, Nanjing University, 210093, P. R. China*
[e] *State Key Laboratory of Alternate Electrical Power System with Renewable Energy Sources, North China Electric Power University, Beijing 102206, P. R. China*

† Electronic supplementary information (ESI) available. See DOI: https://doi.org/10.1039/d3qm00537b

‡ These authors contributed equally to this work.

formed owing to the Lewis-acid base interaction, *i.e.*, iodide in MAI and DMSO act as the Lewis base, and $PbI_2$ as the Lewis acid.[21–25] Afterward, DMSO is evaporated slowly during annealing to retard the rapid reaction between $PbI_2$ and organic iodide. At the beginning of composition engineering research, this adduct ($PbI_2$·MAI·DMSO) was thoroughly studied in $MAPbI_3$ perovskite.[24,26,27] Later, Seok *et al.* manipulated the formation of a Lewis base adduct *via* molecular exchanges between FAI and DMSO.[28] In 2019, Wang *et al.* noticed that even the system of mixed cation perovskite precursors with the MA cation still existed as $PbI_2$··MAI·DMSO.[29,30] They modulated the adduct phase by controlling the ratio of DMSO : DMF and achieved a PCE of over 21% for PSCs.

However, the same solvent engineering method for $FAPbI_3$, which has been applied through different additives, is ineffective as it generates morphological defects in perovskite. For the case of $MAPbI_3$, DMSO could be a good base because it has a common functional group of $-CH_3$. In the case of $FAPbI_3$, the $-NH_2$ functional group results in weak interactions between $NH_2$ and DMSO. As a result, a weaker FAI·DMSO adduct is generated.[31,32] However, $PbI_2$ has a stronger interaction with FAI as compared to MAI or DMSO.[33] Therefore, there are more chances that DMSO detaches from $PbI_2$ and is replaced by FAI. In short, the adduct consists of DMSO and FAI is not as efficient as MAI, so there is a need to develop a facile strategy that can include FAI effectively and form the adduct for mixed cation perovskites. Furthermore, it has been noted that DMSO engages in van der Waals interactions while FAI experiences ionic interactions.[13,28,34] Therefore, the DMSO molecules affixed with $PbI_2$ can be easily replaced by external FAI molecules owing to their higher affinity toward $PbI_2$ relative to DMSO. By taking advantage of this high affinity, herein, the $PbI_2$·MAI·DMSO adduct is modified to $PbI_2$·MAI·FAI·DMSO, and upon annealing the black phase of $MA_xFA_{1-x}PbI_3$ is successfully obtained.[12,26,28] In general, $PbI_2$·MAI·DMSO is usually formed during the spinning process, and $MAPbI_3$ is generated on the chlorobenzene (CB) drop. At this point, the DMSO molecules are replaceable with FAI molecules at low temperatures during spin-coating, especially those DMSO molecules which are lying outside of the adduct.[28–30,34–38] This process successfully replaces DMSO molecules with FAI without any expansion because both the molecules have equal size, hence delivering a PCE of 20.79% for the FAI-treated PSC, which is much higher than that of the pristine $MAPbI_3$-based PSCs (17.43%).[5,29,37] Moreover, on the stability side, modified devices retained 80% of the initial PCE even after 800 h of storage. This increased long-term stability can be attributed to the large grain size of perovskite due to DMSO–FAI molecular interchange. Typically, in $FAPbI_3$ and mixed cation perovskites, the morphology is worse than $MAPbI_3$, which is considered the primary defect whenever the FA is introduced in mixed cation perovskites. However here, the exchange of DMSO with FAI overpassed the inefficient $PbI_2$·FAI·DMSO intermediate phase, and the inclusion of FAI in MAI·FAI·$PbI_2$ at the perfect timing delivered the perovskite film's high crystallinity and large grain sizes. Therefore, the long-term stability was enhanced in $FA_xMA_{1-x}PbI_3$-based PSCs.

## Results and discussion

The proposed mechanism of perovskite formation is schematically illustrated in Fig. 1. For the perovskite precursor solution, we have offered the formation mechanism of the

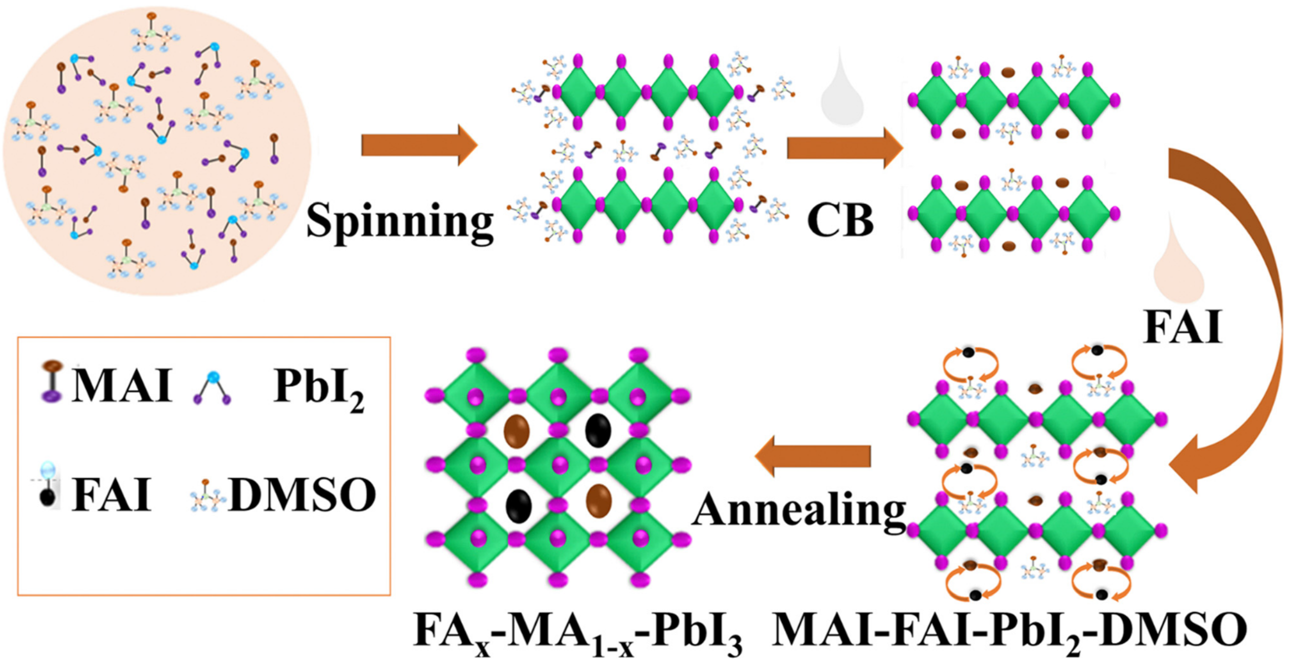

Fig. 1 Schematic of DMSO–FAI molecular interchange to form the $FA_xMA_{1-x}PbI_3$ perovskite.

mixed cation $FA_xMA_{1-x}PbI_3$ perovskite through the molecular exchange of DMSO with FAI, where the obtained perovskite films showed large grain sizes with high crystallinity, resulting in high long-term stability of PSCs. During the preparation of the perovskite precursor, MAI–$PbI_2$ is firstly solubilized with DMF and DMSO, and the adduct of the $PbI_2$·MAI·DMSO perovskite solution was formed during spin-coating. When the ani-solvent CB was dripped on the top of the spin-coating film, the higher affinity of FAI towards $PbI_2$ relative to DMSO in $PbI_2$·MAI·DMSO generally serves as the platform for molecular substitution. After the two-dimensional (2D) MAI·$PbI_2$·DMSO was formed, the FAI/IPA solution was dripped rapidly over the spinning film, where some DMSO molecules were replaced with FAI molecules. As a result, $PbI_2$·MAI·DMSO rapidly transformed into the $PbI_2$·MAI·FAI·DMSO phase through molecular exchange. Basically, the FAI diffused into the 2D structure, and more FAI molecules could easily replace the DMSO molecules at the outer side of the MAI–$PbI_2$–DMSO adduct, while the inner MAI–$PbI_2$–DMSO structure remained unchanged.[28,39] Though in some early published reports, it was claimed that $MA^+$ is replaced with $FA^+$, and both of these ions have different radii.[29,30,34] However, here, the perfect timing of FAI deposition at 2D MAI·$PbI_2$·DMSO facilitates the replacement of DMSO with FAI. Finally, by post-substitution, the pre-deposited MAI·$PbI_2$·DMSO intermediate layer was able to immediately convert into the $FAI_xMAI_{1-x}PbI_2$·DMSO intermediate, which transformed into the $FAI_xMAI_{1-x}PbI_3$ thin film after annealing at 105 °C for 5 minutes and 140 °C for 15 minutes.[21] FAI replaces some MAI sites occupied by DSMO and lead ions need not provide much more coordination points, as shown in Fig. 1. The increased long-term stability of PSCs can be attributed to the large grain size due to DMSO–FAI molecular interchange. FAI involves in the MAI–$PbI_2$–DMSO adduct, resulting in transforming into the black α-phase $FA_xMA_{1-x}PbI_3$ perovskite with larger grain sizes and enhanced crystallinity.

The MAI-based film content in the final perovskite films depends on the concentration of the FAI solution. The step-wise compositional process of the template-assisted perovskite structure can be described as eqn (1).[28,35]

$$PbI_2\cdot MAI\cdot DMSO + FAI \rightarrow MAI\cdot FAI\cdot PbI_2 + DMSO\ (\uparrow \text{removal}) \rightarrow MA_xFA_{1-x}PbI_3 \quad (1)$$

The process described in this article is a novel and efficient method for producing a $FA_xMA_{1-x}PbI_3$ perovskite through adduct modification. The spin-casted MAI·$PbI_2$·DMSO adduct phase is modified through different FAI concentrations. Fig. 2 schematically illustrates the stepwise process of achieving a perovskite film with large grain-sized morphology and high crystal growth *via* adduct transformation. Firstly, the perovskite $PbI_2$·MAI·DMSO precursor solution was prepared using MAI/$PbI_2$ with a molar ratio of 1 : 1 mixed in a DMF/DMSO solution system, and the prepared solution was cast on the FTO/$SnO_2$ substrate.

Then CB as an anti-solvent was slowly dripped on the spin film, and a 2D MAI·$PbI_2$·DMSO intermediate film was formed.[36] After dripping the CB, the spinning substrate was loaded with different FAI/IPA concentrations, followed by thermal

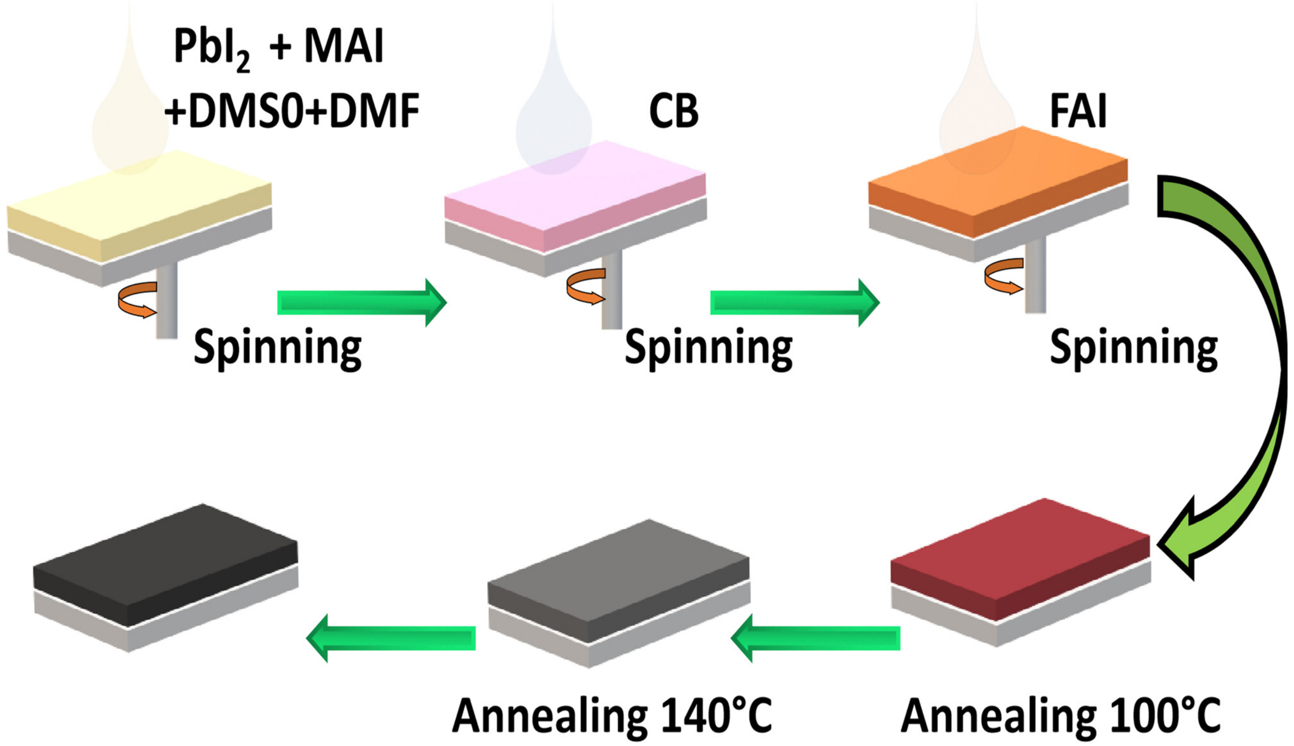

Fig. 2 Schematic illustration of the stepwise process of the mixed perovskite film.

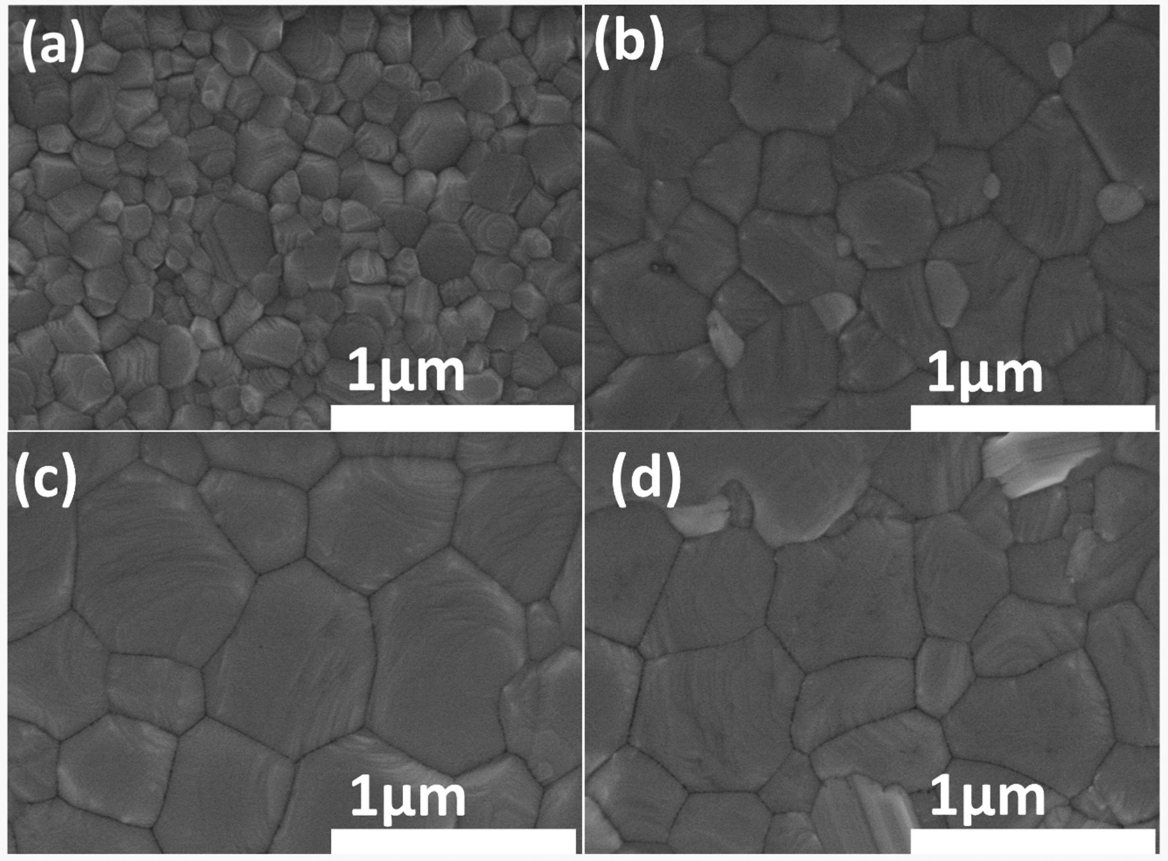

Fig. 3 Surface scanning electron microscopy (SEM) images of the perovskite intermediate adduct modification equipped with varying concentrations of FAI: (a) 0 mg mL$^{-1}$ FAI, (b) 10 mg mL$^{-1}$ FAI, (c) 20 mg mL$^{-1}$ FAI, and (d) 30 mg mL$^{-1}$ FAI.

annealing at 100 °C and 140 °C for the first few seconds and 15 min, respectively. Complete details of the fabrication procedure are described in the experimental materials. The prepared samples are marked as a control (a film without FAI deposition), 10 mg mL$^{-1}$ FAI, 20 mg mL$^{-1}$ FAI and 30 mg mL$^{-1}$ FAI in the Discussion section, where 0 mg mL$^{-1}$, 10 mg mL$^{-1}$, 20 mg mL$^{-1}$, and 30 mg mL$^{-1}$ represent the concentrations of FAI in IPA solutions. To investigate the altered morphologies of modified perovskite films, the texture of the films (with and without FA-treated perovskite) was analyzed through scanning electron microscopy (SEM). The modified perovskite films based on different contents of the FAI/IPA solution are presented in Fig. 3(a)–(d). It is evident that the morphology of the perovskite film with a larger grain size, compactness, and a flat surface is essential for achieving excellent photovoltaic performance.[40,41] It is always difficult to obtain larger grain sizes in FA-based single-cation and mixed-cation perovskite films.[39] Interestingly, when the $MAPbI_3$ surface is loaded with various concentrations of FAI, modifications have been noticed in the surface morphology and grain size of the perovskite films. The control perovskite film showed a random grain distribution with a diverse grain size distribution over the whole layer. On the deposition of 10 mg mL$^{-1}$ FAI/IPA solution, a uniform and compact perovskite layer was obtained with a minute rise in grain size. Notably, 20 mg mL$^{-1}$ film displays an appreciable increase in grain sizes along with a pinhole-free surface, smoothness, and compactness. The comparatively improved morphology of 20 mg mL$^{-1}$-based films could result from the controlled crystallization induced by the FAI-based fine adduct formation. However, when the FAI concentration was increased up to 30 mg mL$^{-1}$, the irregularly shaped grains were noticed.

It is worth seeing that when the FAI concentration was increased, it produced structural stress, which further caused the perovskite grains to shrink and separate.[6,12,37] Thus, the morphological changes provide further evidence that FAI concentration substantially affects the molecular exchange and optimized crystal development of the perovskite film. The average grain sizes of FA-based perovskites were calculated to examine the grain distribution (Fig. S1, ESI1). It is exciting to see that the grain sizes of modified perovskite are straightforwardly linked to the concentrations of FAI. For example, the grain sizes were 270 nm for the control layer and 410 nm for the 10 mg mL$^{-1}$ layer to a maximum value of 695 nm for the 20 mg mL$^{-1}$ film but dropped to 678 nm for the 30 mg mL$^{-1\ \mathrm{film}}$.[12,42] This FAI–DMSO exchange appears to cause efficient recrystallization of the perovskite layer since the quantity of small-sized grains has decreased, and the average perovskite crystal size has visibly grown with a broader size dispersion.[35] On top of that, the atomic force microscopy (AFM) image (Fig. S2, ESI†) reveals that the root mean square roughness values of the films are suppressed on increasing the FAI concentration up to optimized values, i.e., 19.10, 13.5, 10.8, and 17.5 nm for FAI concentrations of 0 mg $mL^{-1}$, 10 mg $mL^{-1}$, 20 mg $mL^{-1}$, and 30 mg $mL^{-1}$, respectively. The film with the optimized FAI concentration (20 mg $mL^{-1}$) was more homogeneous among all.[36,43,44] These microscale measurements of morphological smoothness and uniformity indicate the optimized number of molecular exchanges at an optimal quantity of FAI in the IPA. As a result, it considerably improved the final morphology of the perovskite film. Furthermore, the $FA_xMA_{1-x}PbI_3$–DMSO intermediate phase inhibits the nucleation rate and provides extra time for the grains to evolve, which ultimately results in a homogeneous perovskite layer with larger grains. The larger grain perovskite films were shown to have longer carrier lifetime and lower trap density, owing to the decreased charge buildup and non-radiative recombination resulting from reduced grain boundaries. Consequently, it can be concluded the FAI post-dripping on $MAPbI_3$ before annealing significantly impacts the film's morphology by slowing down the crystallization process.

The crystallinity of perovskite films was measured by X-ray diffraction (XRD) (Fig. 4(a)) to better understand how the incorporation of FAI in 2D $MAI{\cdot}PbI_2{\cdot}DMSO$ affects the final phase of the perovskite film.[45] As expected, a pure tetragonal $MAPbI_3$ phase with a middling peak intensity has been noticed from the results of the XRD diffraction peaks.[41] It can be observed that the crystallinity of perovskite films undergoes a significant improvement after the adduct modification as the peak intensity of the modified film increased, and no noticeable peak shift is seen. The $FA_xMA_{1-x}PbI_3$ synthesized using the suggested approach is stable because no phase transition or breakdown was detected throughout the manufacturing process. In addition, it is shown in Fig. S3 (ESI†) that the (110) peak shifts to a lower degree. Conclusively, the significant changes in the crystal lattice structure of perovskite films following FAI incorporation are continuous with changes in the morphology, as discussed previously.[12,13,37] As shown in Fig. 4(a), we did not find any such lower angle peak in the XRD patterns which can indicate the presence of unreacted FAI on the surface of the perovskite, demonstrating that the dripped amount of FAI solution completely reacts with the pre-deposited film and does not leave behind any unreacted FAI. For lattice parameters that verify the exact ratio of FA to MA in the final perovskite film, here our best perovskite has the FA portion of 50% with the

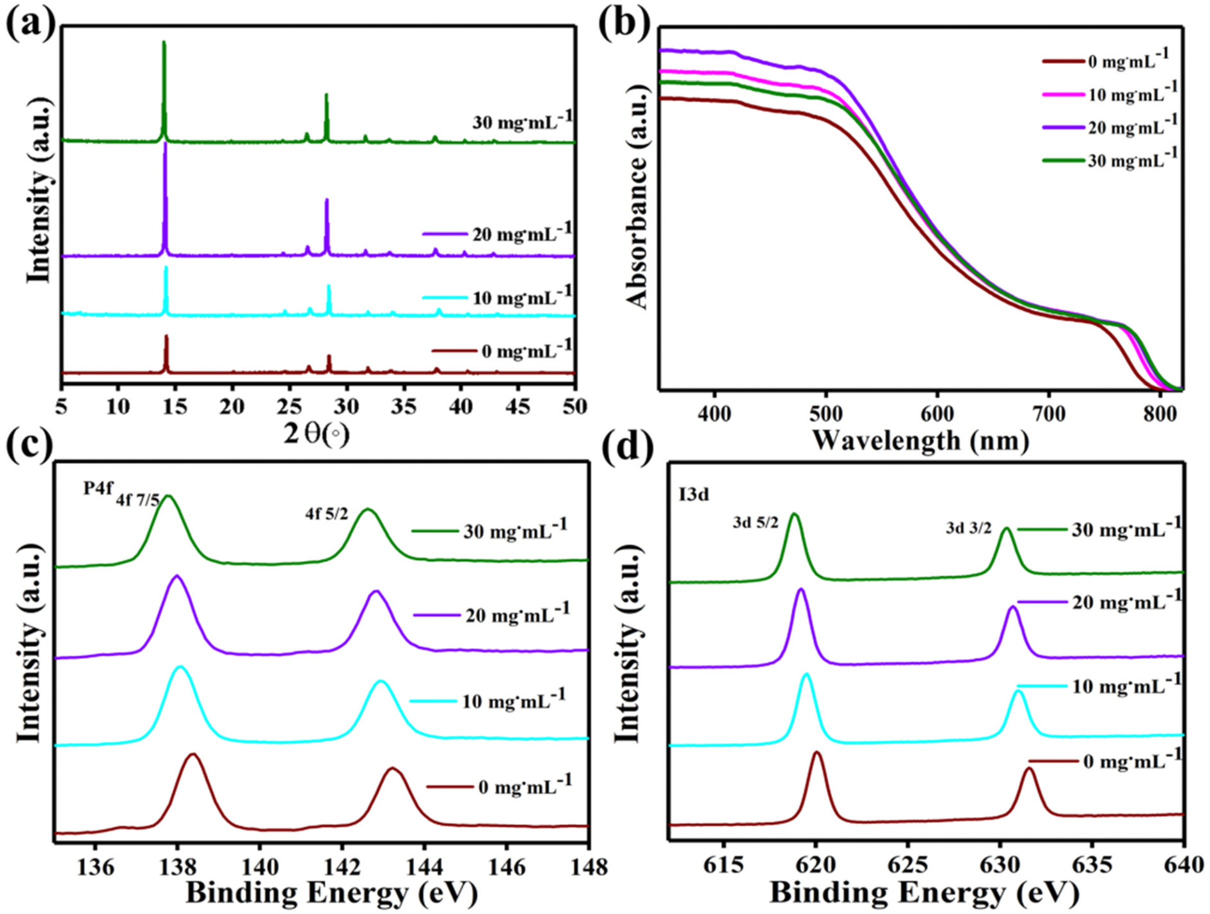

Fig. 4 (a) X-ray diffraction patterns and (b) UV-Vis spectra of the control and FAI-based films with FAI concentrations ranging from 0 mg $mL^{-1}$ to 30 mg $mL^{-1}$. XPS spectra of 0 mg $mL^{-1}$ to 30 mg $mL^{-1}$ FAI-doped perovskites after annealing: (c) Pb 4f and (d) I 3d core spectra of the perovskites with various FAI concentrations.

mixed cations of $FA_{0.57}MA_{0.43}$ for the 20 mg mL$^{-1}$-FAI-based film and we intentionally called it 20 mg mL$^{-1}$-FAI perovskite. We have calculated the lattice parameters of perovskites from the Bragg equation: $2d\sin\theta = n\lambda$ ($\lambda$ = 1.5406 Å), including $MAPbI_3$, and $MAPbI_3$ treated with 10, 20, and 30 mg ml$^{-1}$ FAI, and $FAPbI_3$, as shown in Fig. S4 (ESI†). It is observed that the interplanar crystal spacing of perovskites augments as the concentration of the FAI solution increases linearly, and thus the proportion of MA to FA can be obtained from the figure.[26]

UV-vis absorption spectroscopy results in Fig. 4(b) show the absorption profiles of the perovskite films, revealing the high light absorption of FAI-based films. The 20 mg mL$^{-1}$ FAI perovskite is considerably more robust in absorbing spectrum, followed by the 10 mg mL$^{-1}$ FAI perovskite and the 30 mg mL$^{-1}$ FAI perovskite.[26] The minor degree shift in the absorption edge of the FAI-based profiles indicates FAI incorporation. Fig. S5 (ESI†) also follows a similar trend as the absorption edges of the perovskite film shift with an increment in the FAI concentration. More specifically, when the FAI concentration is increased up to 20 mg mL$^{-1}$, a moderate shift in the absorption edge from ∼795 nm (0 mg mL$^{-1}$) to >800 nm (20 mg mL$^{-1}$) has been noticed.[12,42] The DMSO–FAI smooth exchange in the modified adduct might be responsible for this positive change in the absorption edge, and it is evident that the mixed-cation perovskite film's bandgap ($E_g$) is smaller than that of $MAPbI_3$.

Consequently, the absorption profiles show that the modified films can also absorb photons with lower energy. In comparison, the energy bandgap of pure $MAPbI_3$ is 1.59 eV, whereas that of $FAPbI_3$ is 1.49 eV. Hence, the smooth cation intermixing through molecular exchange boosts the absorption capacity and improves the absorption edge for broader spectrum utilization, resulting in the $J_{SC}$ enhancement of PSCs.

To verify the hypothesis that FAI exchanged with DMSO/MAI alters the Pb–I chemical bonding, X-ray photoelectron spectroscopy (XPS) tests were used, as shown in Fig. 4(c) and (d). Comparing XPS data of FAI deposited and control perovskites, it was realized that the bonding energy of I 3d and Pb 4f shifted to a lower value with an increment in the concentration of FAI. The proof of the change in the binding energy is that the peaks of Pb $4f_{7/2}$ changed from 138.4 to 137.9 eV and the Pb $4f_{5/2}$ peak shifted from 143.3 to 142.7 eV as the FAI concentration increases. According to prior studies, the Pb $4f_{7/2}$ and Pb $4f_{5/2}$ peaks of the pure $MAPbI_3$ perovskite are 137.9 and 143.3 eV, respectively.[45–47] As the Pb 4f and I 3d peaks of the perovskite layer with FAI shift towards lower binding energy, the cationic charge is reduced over Pb and I ions, which could result in lattice structure expansion as noticed in the observations of crystallinity and morphology. Basically, the DMSO and FAI both have similar sizes, which does not lead to lattice expansion. Still, however, some MA cations are replaced by FA, due to which the lattice expands compared to the control perovskite.[12,48]

Moreover, the steady-state photoluminescence (PL) and time-resolved photoluminescence (TRPL) spectra of the control (0 mg mL$^{-1}$) film and FAI-treated (20 mg mL$^{-1}$) films are compared (by depositing both samples on the glass side of the FTO substrate) as shown in Fig. 5(a) and (b). A high intensity with a justified and red shift in the spectrum of the 20 mg mL$^{-1}$ FAI-based film is observed compared to that of the control film, supporting the deposition of 20 mg mL$^{-1}$ FAI

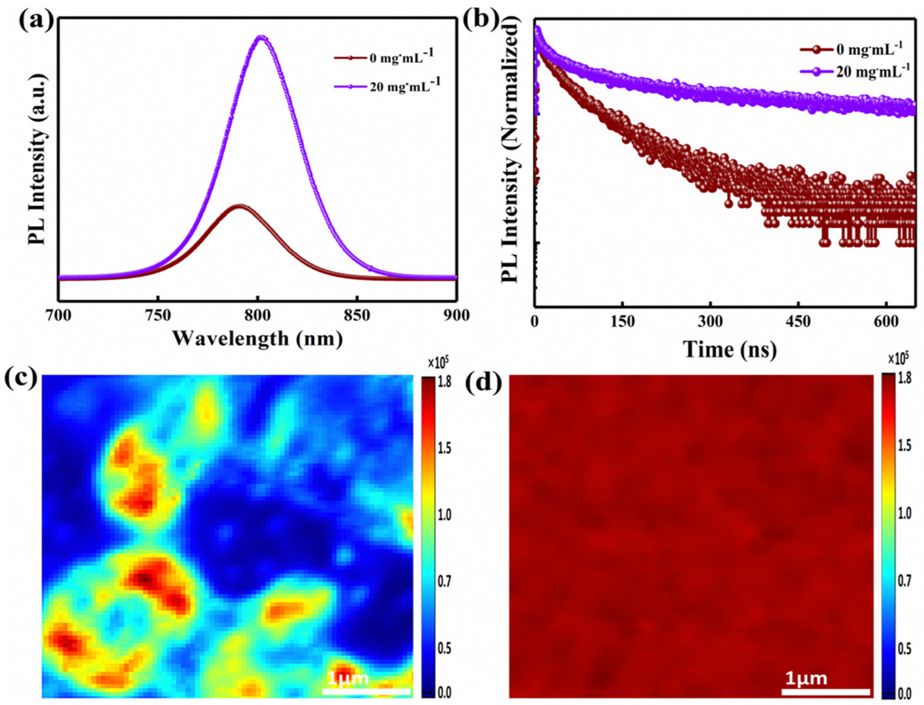

Fig. 5 (a) Steady-state PL spectra and (b) TRPL spectra of control and 20 mg mL$^{-1}$-FAI-based perovskites deposited on the substrate of glass. PL spectral intensity mapping images of (c) control and (d) 20 mg mL$^{-1}$-FAI-based films on the glass substrates.

reduces the bandgap of the perovskite film.[12,26] The improvement in the PL response indicates that the DMSO–FAI exchange resulted in a well-engineered mixed perovskite crystal ($FA_xMA_{1-x}PbI_3$) in bulk and at the interface, hindering the deep-level traps in bulk areas of the perovskite film. As a consequence, the non-radiative recombination of charge carriers is greatly suppressed. A double bi-exponential model is applied to fit the TRPL decay curve for the calculations of the carrier lifetime (eqn (2)). In addition, eqn (3) was used to find the average PL decay time ($\tau_{ave}$).[39,49,50]

$$f(t) = \sum_i A_i \exp\cdot\left(-\frac{t}{\tau_i}\right) + f_0 \tag{2}$$

$$\tau_{ave} = \frac{\sum A_i \tau_i^2}{\sum A_i \tau_i} \tag{3}$$

where $A$, $\tau$, and $f_0$ are the decay amplitude, the decay time, and the constant. The carrier lifetimes obtained from the TRPL are shown in Table S1 (ESI†). The decay curves can be separated into two parts: a fast decay ($\tau_1$) and a slow decay ($\tau_2$). $\tau_1$ represents non-radiative interface recombination, while $\tau_2$ is associated with trap-assisted recombination in the perovskite bulk.[12] The 20 mg mL$^{-1}$-FAI film exhibited a $\tau_{avg}$ (average carrier lifetime) value of 88.33 ns, while the control film showed a lower $\tau_{avg}$ value of 70.01 ns. The increment in the $\tau_{avg}$ values of the 20 mg mL$^{-1}$-FAI-based film hints at an improved carrier lifetime and can be ascribed to the fewer grain boundaries and trap sites.[4,50,51] The PL intensity mappings of control and 20 mg mL$^{-1}$-FAI based perovskites are shown in Fig. 5(c) and (d), which gives a better understanding of the charge-carrier dynamics. The control film exhibits a non-uniform peak intensity stimulated by the more significant trap flux. In contrast, the 20 mg mL$^{-1}$-FAI based film shows uniform and high peak intensity, which suggests that non-radiative exciton decay is minimized.

Fig. 6(a) illustrates the device architecture with the structure of glass/FTO/compact-$SnO_2$/perovskite/spiro-OMeTAD/Au. A cross-sectional SEM figure of the final 20 mg mL$^{-1}$-FAI prepared device is shown in Fig. 6(b). To investigate the photoelectric performance of the fabricated devices with different concentrations of FAI, *J–V* curves were measured in the ambient environment, as presented in Fig. 6(c) and (d). The PV characteristics of the control and FAI-based PSCs with various concentrations are described in Table 1. The 0 mg mL$^{-1}$ device showed a PCE of 18.13% with $V_{OC}$ of 1.05 V, $J_{SC}$ of 23.02 mA cm$^{-2}$, and FF of 74.04% under reverse scan, while achieving a 16.14% PCE under forward scan In contrast, the 20 mg mL$^{-1}$-FAI treated PSC achieved a PCE of 20.79% with a $V_{OC}$ of 1.10 V, $J_{SC}$ of 23.89 mA cm$^{-2}$, and FF of 78.07% under reverse scan, while delivering a proximate PCE of 20.03% under forward scan. All these improvements have resulted from improved crystallization. The $V_{OC}$ is enhanced due to optimized FAI–DMSO interchanging and decreased interfacial recombination, thus improving the PCE of modified devices. The reduction in charge accumulation at the interface also helped in the increment of FF, and the slight improvement in $J_{SC}$ can be attributed to the low band gap of the mixed cation perovskites. Conclusively, the adduct modification through FAI–DMSO exchange is a reliable technique for obtaining mixed-cation-based perovskites.[12,39] However, when the FAI concentration is further increased over the optimum value, the perovskite film undergoes deterioration, most likely owing to

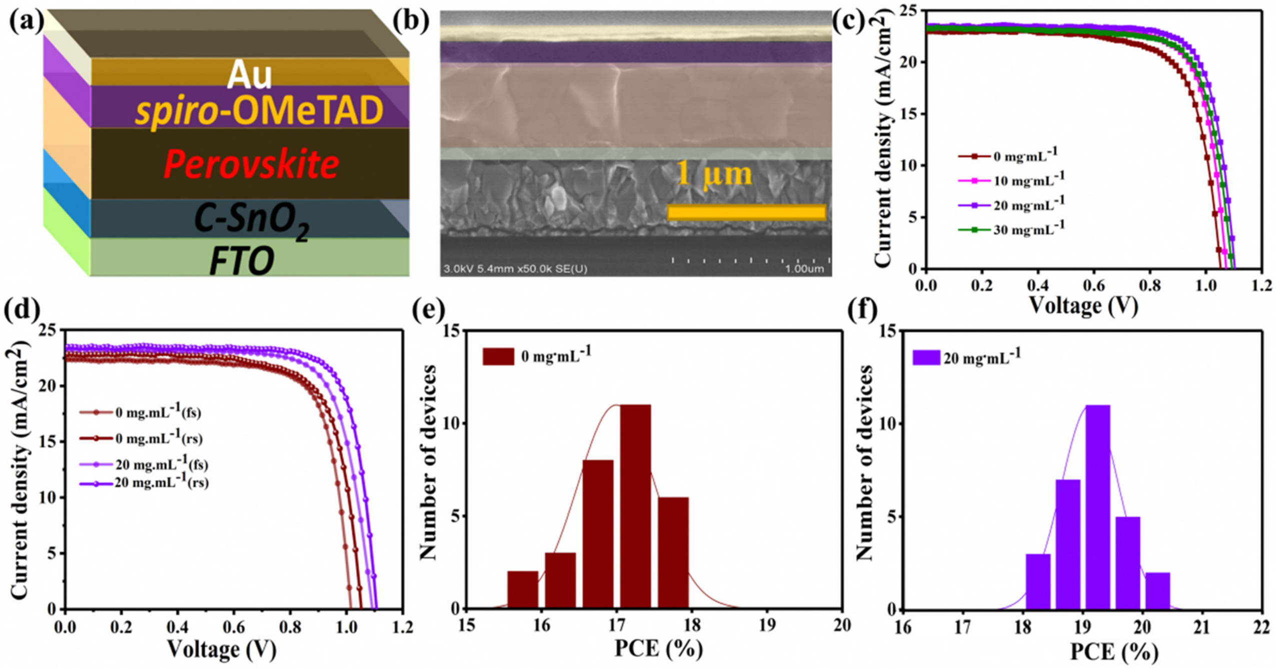

Fig. 6 (a) Device architecture and (b) cross-sectional SEM image of the 20 mg mL$^{-1}$-FAI PSC. (c) *J–V* curves for the best-performing PSCs with various FAI concentrations. (d) *J–V* curves of control and 20 mg mL$^{-1}$-FAI treated PSCs with reverse and forward scans. Distribution PCE of (e) 0 mg mL$^{-1}$ and (f) 20 mg mL$^{-1}$-FAI treated devices. There are 30 and 28 devices of the statistical distribution of PCEs for control and 20 mg mL$^{-1}$-FAI PSCs.

Table 1 The parameters of PSCs with different concentrations of FAI

| Devices | $J_{SC}$ (mA cm$^{-2}$) | $V_{OC}$ (V) | FF (%) | PCE (%) |
|---|---|---|---|---|
| 0 mg mL$^{-1}$ | 23.02 | 1.05 | 74.04 | 18.13 |
| 10 mg mL$^{-1}$ | 23.13 | 1.07 | 76.07 | 19.23 |
| 20 mg mL$^{-1}$ | 23.89 | 1.10 | 78.07 | 20.79 |
| 30 mg mL$^{-1}$ | 23.55 | 1.09 | 77.35 | 19.87 |

the perovskite's crystal disruptions. Therefore, the 30 mg mL$^{-1}$-FAI device exhibits inferior performance.

Furthermore, Fig. 6(d) shows that the device with 20 mg mL$^{-1}$-FAI exhibits a low hysteresis that can be attributed to the reduced deep-level traps and decreased interfacial recombination.[2,26]

Moreover, the statistical distribution of PCEs of more than 20 cells from both methods also exhibits that the 20 mg mL$^{-1}$-FAI-based devices perform better, as shown in Fig. 6(e) and (f). Incident photo-current conversion efficiency (IPCE) spectra define the variation in photo-currents measured from various devices (Fig. 7(a)). It is indeed clear from IPCE curves that the devices have a different spectrum behavior, as the 20 mg mL$^{-1}$-based device shows a significantly increased photon-to-electron conversion efficiency in much of the reactive spectral region when compared to the standard device, which is consistent with the pattern shown in the *J*–*V* curve. There are two possible explanations for the higher IPCE in the 20 mg mL$^{-1}$-FAI treated device. First, the proposed transitional procedure results in a compact film that is both uniform and persistent, leading to suppression of the nonradiative recombination. Second, the UV-vis absorption spectra demonstrate that uniform film coverage significantly increases visible-light absorption through the absorber layer, thus increasing $J_{SC}$.[2,36]

Open-circuit voltage decay (OCVD) is typically used to investigate the anode's charge recombination and electron mobility processes against the photo spectral response. The photovoltage decay curves of Fig. 7(b) show that the $V_{OC}$ value decreases rapidly in the control device, which further indicates serious non-irradiative recombination, while the 20 mg mL$^{-1}$ device shows a steady behavior over time. The carrier (*i.e.*, electron) lifetime $\tau$ is determined *via* eqn (4), and plotted in Fig. 7(c).

$$\tau_n = -k_BTe^{-1}/(qV_{oc}/dt)^{-1} \tag{4}$$

The $k_B$, $T$, and $e$ represent the Boltzmann constant, absolute temperature, and elementary charge, respectively. The electron lifetime is directly related to the FAI concentrations. Apparently, the 20 mg mL$^{-1}$-FAI PSC achieves a longer $\tau_n$ compared to the control PSC, demonstrating that the 20 mg mL$^{-1}$ device has a suppressed charge recombination rate, which is accredited to the enhanced crystallinity and abridged trap density of the $FA_xMA_{1-x}PbI_3$ film.[12,30,39] This efficient charge transport in the device can be attributed to the positive morphological changes in the perovskite film, which obviously helped in charge separation, selection, and charge transport processes. The space-charge-limited-current (SCLC) method was utilized to examine the trap state densities of the prepared films, as shown in Fig. S5a and b (ESI†). The device structure of glass/FTO/c-$SnO_2$/perovskite/PCBM/Au was used for the measurement of

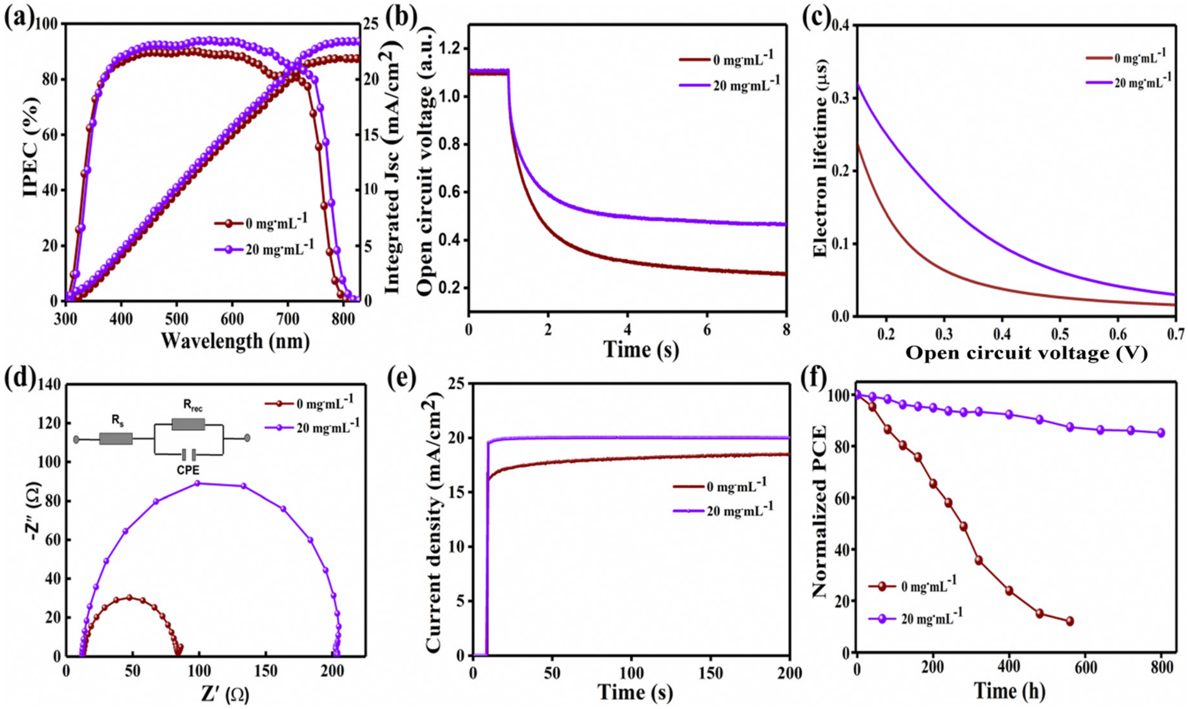

Fig. 7 Comparisons of the control and 20 mg mL$^{-1}$-FAI based devices: (a) IPCE spectra, (b) transient photo-voltage decays, (c) electron lifetime and $V_{OC}$ correlation, (d) electrochemical impedance spectroscopy (EIS) with Nyquist plot, (e) stabilized current density at the maximum power point (MPP), and (f) normalized PCE attenuation under 30% relative humidity and 25 °C for about 800 h.

SCLC.[49] The fitting curves (Fig. S6, ESI†) extract the trap-filled limit voltage ($V_{\mathrm{TFL}}$), pointed by the conversion from the ohmic area to the TFL area. Eqn (5) can be utilized to calculate the trap state density of perovskites.[3,12]

$$n_{\mathrm{t}} = 2\varepsilon_0\varepsilon_{\mathrm{r}}\cdot V_{\mathrm{TFL}}/eL^2 \tag{5}$$

The $2\varepsilon_0\varepsilon_{\mathrm{r}}/eL^2$ is constant for the same materials, and the trap density ($n_{\mathrm{t}}$) is directly proportional to $V_{\mathrm{TFL}}$.[52] The 20 mg mL$^{-1}$ films showed an abridged onset voltage of trap-filled limit and consequentially reduced defect density. The determined $V_{\mathrm{TFL}}$ values for the control and 20 mg mL$^{-1}$ optimized samples are 0.228 V and 0.146 V, respectively. The trap density of the 20 mg mL$^{-1}$ device is lower than that of the control device, which could be attributed to the controlled crystallization through adduct phase modification, resulting in the high FF and $V_{\mathrm{OC}}$ values.[12,39]

In order to obtain rich interfacial information, such as the electron transport process and contact resistance in PSCs, electrochemical impedance spectroscopy (EIS) is applied, as shown in Fig. 7(d).[4] Series resistance ($R_{\mathrm{S}}$) is approximately equal for the control and 20 mg mL$^{-1}$-FAI-based devices. Fig. 7(d) illustrates an equivalent circuit model through which the charge transfer resistance is extrapolated. Recombination resistance ($R_{\mathrm{rec}}$) is larger in the 20 mg mL$^{-1}$-FAI film than that in the control one, suggesting that the recombination is significantly reduced in the 20 mg mL$^{-1}$-FAI-based device. This hindrance in the recombination is due to the intensified carrier flow between the perovskite and charge transporting layers.[24] The enhanced $R_{\mathrm{rec}}$ helps in boosting the photovoltaic performance through effective charge separation at the respective collection layer. To investigate the stabilized power output of PSCs, maximum power point tracking was measured sustaining 200 s for 0 mg mL$^{-1}$ and 20 mg mL$^{-1}$–FAI based devices. The 20 mg mL$^{-1}$-FAI based device exhibits an excellent stable power output (SPO) of 18.43% at a bias voltage of 0.920 V, compared with 16.58% of SPO for the control device at a bias voltage of 0.878 V, as presented in Fig. 7(e). The perovskite device based on 20 mg mL$^{-1}$-FAI shows a substantially faster reaction, most likely because of the low hysteresis and internal losses.[25,45]

The crystallization factor is considered one of the major reasons behind the instability of the PSCs, which is a big commercialization hurdle. Hence, herein, the recrystallization of perovskite through adduct modification improved the long-term stabilities, which can be seen in Fig. 7(f). The PCE value of the control device gradually reduced to nearly 10% after 600 hours of aging. Conversely, the device based on 20 mg mL$^{-1}$-FAI maintained more than 80% of initial efficiency for 800 hours. The lengthened life span of the 20 mg mL$^{-1}$-FAI-based device can be attributed to the smooth film formation without any noticeable loophole, preventing any ambient species from intercalating into the active layer.[53,54] Consequently, adduct control during the crystallization phase for the perovskite layer not only enhances the perovskite layer crystal quality with large grains and suppressed defects but can also exhibit the excellent stability of the perovskite layer, indirectly reducing the trap-assisted recombination and leading to a high performable PSCs. The long life span of the 20 mg mL$^{-1}$ device indicates that adduct modification *via* intermediate engineering is an effective technique to improve the morphology of the perovskite film, which is the main barrier in scaling up the fabrication methods of PSCs.[26,52,55]

## Conclusion

As the PSCs are entering the industrialization mode, the large area fabrication through industrial methods is a big challenge where the mixed perovskites are facing the issues of high-quality morphology and crystallinity. Therefore, novel methods for obtaining perovskite films with large grain sizes and good crystallinity are in demand. The optimized controlling of perovskite crystallization implies the improved crystallinity and morphology of perovskite films, which generally provides high efficiency and a long life span to PSCs. In this work, a novel method of adduct control is presented for mixed cation PSCs where the FAI dexterously takes the place of DMSO in the $PbI_2$·MAI·DMSO adduct through intermolecular exchange. As a result, perovskite films with large-size grains are obtained, which not only enhances the PCE but also improves the long-term stability of PSCs.

## Experimental

### Materials

A tin(IV) oxide colloidal dispersion (at 15% concentration) in water was acquired from Alfa Aesar to prepare a $SnO_2$ colloidal dispersion. The $SnO_2$ solution was diluted with deionized water to a concentration of 2.5% before being used and then stirred for 1 hour at room temperature. Fluorine-doped $SnO_2$-coated (FTO) glass substrates with a thickness of 2.2 mm were acquired from China for the PSCs. Lead iodide ($PbI_2$, purity is >99.99%), formamidinium iodide (FAI), methylammonium iodide (MAI, purity is greater >99.5%), and Spiro-OMeTAD were bought from Xian polymer light technology corporation. Other different solvents (anhydrous) such as chlorobenzene (CB), dimethyl sulfoxide (DMSO, 99.9%), dimethylformamide (DMF), and isopropyl alcohol (IPA, purity is >99.5%) were bought from Sigma-Aldrich. Lithium bis(trifluoromethyl sulphonyl)imide (Li-TFSI) and 4-terstbutypridine (tBP) were bought from Aldrich (U.S.). All of these commercially accessible substances were utilized in their unprocessed form. All of the solvents and chemicals will be stored in a glove box until we were ready to begin the experiment.

### Device fabrication

FTO glass with a resistance sheet of 15 Ω sq$^{-1}$ was etched by using zinc powder and HCl. The substrate was cleaned twice ultrasonically in detergent, DI water, acetone (CAN), and isopropanol (IPA) for 20 min sequentially, and all substrates were dried with nitrogen and cleaned with UV ozone for 30 minutes. $SnO_2$ was spin-coated onto FTO glass at 5000 rpm for 30 s.

Then, the substrates were annealed on a hot plate at 150 °C for 30 min in ambient air. All substrates were UV ozone for 30 minutes subsequently. A precursor solution of $MAPbI_3$ perovskite was prepared by mixing 461 mg of $PbI_2$ and 159 mg of MAI in the DMF : DMSO (4 : 1) solvent and stirring at 60 °C for 60 min. Perovskite solution was spin-coating on the substrate (FTO/$SnO_2$) at 5500 rpm for 40 s and 150 μL of chlorobenzene (CB) was dripped at the center of the rotating film within 10 s. During spin-coating afterward, 40 μL of FAI in IPA solution was used for intermediate engineering, dripping on the $PbI_2$–MAI–DMSO intermediate phase with different concentrations of FAI such as 0, 15, 20, and 30 mg $mL^{-1}$, respectively. Once the FAI solution was dripped over the under-developed film, the thin transparent layer suddenly turned blackish-red. Finally, FAI-based perovskites were annealed at 100 °C for 5 minutes, during which time their color changed to dark brown; after another 30 minutes of annealing at 140 °C, the films went completely black. We did not find any changes in the thickness of the perovskite layer after the treatment of FAI. A solution was combined with spiro-OMeTAD (73 mg), CB (1 milliliter), Li-TFSI (17.5 microliters), and 4-*tert*-butylpyridine (28 microliters) to create a hole transport material. 25 μL of the spiro-OMeTAD solution was spin-coated at 5000 rpm for 30 s on the perovskite film surface. A 60 nm thick Au electrode layer was deposited on the perovskite film by thermal evaporation in a vacuum.

### Characterization

In order to investigate the morphology, a scanning electron microscope (Hitachi SU8010; Tokyo, Japan) was used. The XPS spectra were recorded using a Thermo Fisher Scientific ESCALAB 250XI X-ray spectrometer (Shanghai, China). Using X-ray diffraction with Cu K beam radiation at 0.15406 nm, the crystallinity of perovskites was determined (X'Pert Pro, Almelo, the Netherlands). The absorption spectra of perovskites were recorded using a UV-Vis spectrophotometer (SOLID 3700, SHIMADZU, Tokyo, Japan). An Edinburgh PLS980 was used to analyze the produced samples' steady-state PL spectra (Edinburgh Instruments Ltd, Edinburgh, UK). A laser confocal Raman spectrometer (Princeton Instruments, Acton Standard Series SP-2558, Edinburgh Instruments Ltd, Edinburgh, UK). An FLS980 steady-state/transient fluorescence spectrometer was used to record TRPL readings (Edinburgh Instruments Ltd, Edinburgh, UK). *J*–*V* characteristic curves were obtained by scanning forward (−0.1 to 1.2 V) and backward (1.2 to −0.1 V) under AM 1.5 G solar illumination at 100 mW $cm^{-2}$. A solar simulator that was fitted with a Keithley 2400 source meter (94043A, Oriel Instruments, Franklin, Massachusetts, United States) was calibrated using a silicon cell in an atmosphere composed of nitrogen. To prevent light scattering and to demarcate the active region, the solar cells were covered with a black cap of 0.09 $cm^2$ area. Using ZSim-version 3.20 software, an equivalent circuit was fitted to the EIS data. Electrochemical impedance spectroscopy (EIS) measurements were taken from 10 MHz to 1 MHz using a Zahner electrochemical workstation (Zahner Zennium, Kronach, Germany). Z-view ZSim-software version 3.20 with similar circuit modeling software was utilized to conduct the analysis of the impedance data. The EQE spectra were recorded by employing a spectrally-resolved 300 W Xenon lamp with a 5 nm order-sorting filter (Oriel Instruments, Franklin, MA, USA).

## Conflicts of interest

There are no conflicts to declare.

## Acknowledgements

Muhammad Ma-teen and Ziyu Li contributed equally to this work. This work was supported by the Key Research and Development Program of Zhejiang Province (2021C01006), the Scientific Research Fund of Zhejiang Provincial Education Department (Y202147258), the National Key R&D Program of China (2018YFB1500102), the Zhejiang Provincial Natural Science Foundation of China (No. LQ18F040002, LY17F040001) and the Zhejiang Provincial Key Laboratory (No. 2013E10022).

## References

1 N.-G. Park and K. Zhu, Scalable fabrication and coating methods for perovskite solar cells and solar modules, *Nat. Rev. Mater.*, 2020, **5**, 333–350.

2 J. J. Yoo, G. Seo, M. R. Chua, T. G. Park, Y. Lu, F. Rotermund, Y.-K. Kim, C. S. Moon, N. J. Jeon and J.-P. Correa-Baena, Efficient perovskite solar cells *via* improved carrier management, *Nature*, 2021, **590**, 587–593.

3 H. Chen, Y. Chen, T. Zhang, X. Liu, X. Wang and Y. Zhao, Advances to high-performance black-phase $FAPbI_3$ perovskite for efficient and stable photovoltaics, *Small Struct.*, 2021, **2**, 2000130.

4 M. Mateen, Z. Arain, X. Liu, C. Liu, Y. Yang, Y. Ding, S. Ma, Y. Ren, Y. Wu and Y. Tao, High-performance mixed-cation mixed-halide perovskite solar cells enabled by a facile intermediate engineering technique, *J. Power Sources*, 2020, **448**, 227386.

5 J. Jeong, M. Kim, J. Seo, H. Lu, P. Ahlawat, A. Mishra, Y. Yang, M. A. Hope, F. T. Eickemeyer and M. Kim, Pseudo-halide anion engineering for α-$FAPbI_3$ perovskite solar cells, *Nature*, 2021, **592**, 381–385.

6 M. M. Byranvand, C. Otero-Martínez, J. Ye, W. Zuo, L. Manna, M. Saliba, R. L. Hoye and L. Polavarapu, Recent Progress in Mixed A-Site Cation Halide Perovskite Thin-films and Nanocrystals for Solar Cells and Light-Emitting Diodes, *Adv. Opt. Mater.*, 2022, **10**, 2200423.

7 F. Xu, T. Zhang, G. Li and Y. Zhao, Mixed cation hybrid lead halide perovskites with enhanced performance and stability, *J. Mater. Chem. A*, 2017, **5**, 11450–11461.

8 R. Swartwout, M. T. Hoerantner and V. Bulović, Scalable deposition methods for large-area production of perovskite thin films, *Energy Environ. Mater.*, 2019, **2**, 119–145.

9 S. Sajid, S. Khan, A. Khan, D. Khan, A. Issakhov and J. Park, Antisolvent-fumigated grain growth of active layer for efficient perovskite solar cells, *Sol. Energy*, 2021, **225**, 1001–1008.

10 Z. Arain, C. Liu, Y. Yang, M. Mateen, Y. Ren, Y. Ding, X. Liu, Z. Ali, M. Kumar and S. Dai, Elucidating the dynamics of solvent engineering for perovskite solar cells, *Sci. China Mater.*, 2019, **62**, 161–172.

11 J. A. S. Syed, D. Khan, W. Ahmad, G. S. Soomro and A. A. Dar, Formamidinium post-dripping on methylammonium lead iodide to achieve stable and efficient perovskite solar cells, *Int. J. Energy Res.*, 2022, **46**, 5306–5314.

12 M. Mateen, Z. Arain, C. Liu, Y. Yang, X. Liu, Y. Ding, P. Shi, Y. Ren, Y. Wu and S. Dai, High-Quality $(FA)_x(MA)_{1-x}PbI_3$ for Efficient Perovskite Solar Cells *via* a Facile Cation-Intermixing Technique, *ACS Sustainable Chem. Eng.*, 2019, **7**, 11760–11768.

13 S. Chen, X. Xiao, B. Chen, L. L. Kelly, J. Zhao, Y. Lin, M. F. Toney and J. Huang, Crystallization in one-step solution deposition of perovskite films: Upward or downward?, *Sci. Adv.*, 2021, **7**, eabb2412.

14 H. Sun, K. Deng, Y. Zhu, M. Liao, J. Xiong, Y. Li and L. Li, A novel conductive mesoporous layer with a dynamic two-step deposition strategy boosts efficiency of perovskite solar cells to 20%, *Adv. Mater.*, 2018, **30**, 1801935.

15 P. Zhao, B. J. Kim, X. Ren, D. G. Lee, G. J. Bang, J. B. Jeon, W. B. Kim and H. S. Jung, Antisolvent with an ultrawide processing window for the one-step fabrication of efficient and large-area perovskite solar cells, *Adv. Mater.*, 2018, **30**, 1802763.

16 X. Zheng, B. Chen, J. Dai, Y. Fang, Y. Bai, Y. Lin, H. Wei, X. C. Zeng and J. Huang, Defect passivation in hybrid perovskite solar cells using quaternary ammonium halide anions and cations, *Nat. Energy*, 2017, **2**, 1–9.

17 G. Qu, D. Khan, F. Yan, A. Atsay, H. Xiao, Q. Chen, H. Xu, I. Nar and Z.-X. Xu, Reformation of thiophene-functionalized phthalocyanine isomers for defect passivation to achieve stable and efficient perovskite solar cells, *J. Energy Chem.*, 2022, **67**, 263–275.

18 D. Khan, X. Liu, G. Qu, A. R. Nath, P. Xie and Z. X. Xu, Nexuses Between the Chemical Design and Performance of Small Molecule Dopant-Free Hole Transporting Materials in Perovskite Solar Cells, *Small*, 2023, **19**, 2205926.

19 E. Rezaee, D. Khan, S. Cai, L. Dong, H. Xiao, S. R. P. Silva, X. Liu and Z.-X. Xu, Phthalocyanine in perovskite solar cells: A review, *Mater. Chem. Front.*, 2023, **7**, 1704–1736.

20 G. Qu, L. Dong, Y. Qiao, D. Khan, Q. Chen, P. Xie, X. Yu, X. Liu, Y. Wang and J. Chen, Dopant-Free Phthalocyanine Hole Conductor with Thermal-Induced Holistic Passivation for Stable Perovskite Solar Cells with 23% Efficiency, *Adv. Funct. Mater.*, 2022, **32**, 2206585.

21 P. Zhao, B. J. Kim and H. S. Jung, Passivation in perovskite solar cells: A review, *Mater. Today Energy*, 2018, **7**, 267–286.

22 W. Xiang, J. Zhang, S. F. Liu, S. Albrecht, A. Hagfeldt and Z. Wang, Intermediate phase engineering of halide perovskites for photovoltaics, *Joule*, 2021, **6**, 315–339.

23 Z. Arain, C. Liu, Y. Ren, Y. Yang, M. Mateen, X. Liu, Y. Ding, Z. Ali, X. Liu and S. Dai, Low-temperature annealed perovskite films: A trade-off between fast and retarded crystallization *via* solvent engineering, *ACS Appl. Mater. Interfaces*, 2019, **11**, 16704–16712.

24 W. S. Yang, J. H. Noh, N. J. Jeon, Y. C. Kim, S. Ryu, J. Seo and S. I. Seok, High-performance photovoltaic perovskite layers fabricated through intramolecular exchange, *Science*, 2015, **348**, 1234–1237.

25 J. Sin, H. Kim, M. Kim, M. Kim, J. Shin, J. Hong and J. Yang, Anti-solvent treatment time approach to high efficiency perovskite solar cells with temperature of coating environmental, *Sol. Energy Mater. Sol. Cells*, 2023, **250**, 112054.

26 P. Shi, Y. Ding, Y. Ren, X. Shi, Z. Arain, C. Liu, X. Liu, M. Cai, G. Cao and M. K. Nazeeruddin, Template-Assisted Formation of High-Quality α-Phase $HC(NH_2)_2PbI_3$ Perovskite Solar Cells, *Adv. Sci.*, 2019, **6**, 1901591.

27 H. Shi, L. Zhang, H. Huang, Y. Ou, X. Wang, Z. Li, D. Chi and S. Huang, Additive Engineering for High-Performance Two-Dimensional Dion–Jacobson Pb–Sn Alloyed Perovskite Solar Cells, *Energy Technol.*, 2022, 2200983.

28 N. J. Jeon, J. H. Noh, Y. C. Kim, W. S. Yang, S. Ryu and S. I. Seok, Solvent engineering for high-performance inorganic–organic hybrid perovskite solar cells, *Nat. Mater.*, 2014, **13**, 897–903.

29 M. Wang, F. Cao, K. Deng and L. Li, Adduct phases induced controlled crystallization for mixed-cation perovskite solar cells with efficiency over 21%, *Nano Energy*, 2019, **63**, 103867.

30 P. Shi, Y. Ding, C. Liu, Y. Yang, Z. Arain, M. Cai, Y. Ren, T. Hayat, A. Alsaedi and S. Dai, Advanced partial nucleation for single-phase $FA_{0.92}MA_{0.08}PbI_3$-based high-efficiency perovskite solar cells, *Sci. China Mater.*, 2019, **62**, 1846–1856.

31 F. Yang, L. Dong, D. Jang, K. C. Tam, K. Zhang, N. Li, F. Guo, C. Li, C. Arrive, M. Bertrand, C. J. Brabec and H. J. Egelhaaf, Fully Solution Processed Pure α-Phase Formamidinium Lead Iodide Perovskite Solar Cells for Scalable Production in Ambient Condition, *Adv. Energy Mater.*, 2020, **10**, 2001869.

32 J. W. Lee, Z. Dai, C. Lee, H. M. Lee, T. H. Han, N. De Marco, O. Lin, C. S. Choi, B. Dunn, J. Koh, D. Di Carlo, J. H. Ko, H. D. Maynard and Y. Yang, Tuning Molecular Interactions for Highly Reproducible and Efficient Formamidinium Perovskite Solar Cells *via* Adduct Approach, *J. Am. Chem. Soc.*, 2018, **140**, 6317–6324.

33 W. S. Yang, J. H. Noh, N. J. Jeon, Y. C. Kim, S. Ryu, J. Seo and S. I. Seok, High-performance photovoltaic perovskite layers fabricated through intramolecular exchange, *Science*, 2018, **348**, 1234–1237.

34 M. Kroll, S. D. Öz, Z. Zhang, R. Ji, T. Schramm, T. Antrack, Y. Vaynzof, S. Olthof and K. Leo, Insights into the evaporation behaviour of FAI: material degradation and consequences for perovskite solar cells, *Sustainable Energy Fuels*, 2022, **6**, 3230–3239.

35 G. Wu, H. Li, J. Cui, Y. Zhang, S. Olthof, S. Chen, Z. Liu, D. Wang and S. Liu, Solvent engineering using a volatile solid for highly efficient and stable perovskite solar cells, *Adv. Sci.*, 2020, **7**, 1903250.

36 M. Mateen, Z. Arain, Y. Yang, X. Liu, S. Ma, C. Liu, Y. Ding, X. Ding, M. Cai and S. Dai, MACl-induced intermediate engineering for high-performance mixed-cation perovskite solar cells, *ACS Appl. Mater. Interfaces*, 2020, **12**, 10535–10543.

37 Y. Zou, H. Y. Wang, Y. Qin, C. Mu, Q. Li, D. Xu and J. P. Zhang, Reduced Defects of $MAPbI_3$ Thin Films Treated by FAI for High-Performance Planar Perovskite Solar Cells, *Adv. Funct. Mater.*, 2019, **29**, 1805810.

38 R. Wang, J. Xue, K.-L. Wang, Z.-K. Wang, Y. Luo, D. Fenning, G. Xu, S. Nuryyeva, T. Huang and Y. Zhao, Constructive molecular configurations for surface-defect passivation of perovskite photovoltaics, *Science*, 2019, **366**, 1509–1513.

39 P. Shi, Y. Ding, C. Liu, Y. Yang, Z. Arain, M. Cai, Y. Ren, T. Hayat, A. Alsaedi and S. Dai, Advanced partial nucleation for single-phase $FA_{0.92}MA_{0.08}PbI_3$-based high-efficiency perovskite solar cells, *Sci. China Mater.*, 2019, **62**, 1846–1856.

40 S. Sajid, S. Alzahmi, I. B. Salem and I. M. Obaidat, Perovskite-Surface-Confined Grain Growth for High-Performance Perovskite Solar Cells, *Nanomaterials*, 2022, **12**, 3352.

41 M. Kim, G.-H. Kim, T. K. Lee, I. W. Choi, H. W. Choi, Y. Jo, Y. J. Yoon, J. W. Kim, J. Lee and D. Huh, Methylammonium chloride induces intermediate phase stabilization for efficient perovskite solar cells, *Joule*, 2019, **3**, 2179–2192.

42 D. Bi, J. Luo, F. Zhang, A. Magrez, E. N. Athanasopoulou, A. Hagfeldt and M. Grätzel, Morphology engineering: A route to highly reproducible and high efficiency perovskite solar cells, *ChemSusChem*, 2017, **10**, 1624–1630.

43 J. Chen, J. Xu, L. Xiao, B. Zhang, S. Dai and J. Yao, Mixed-Organic-Cation $(FA)_x(MA)_{1-x}PbI_3$ Planar Perovskite Solar Cells with 16.48% Efficiency *via* a Low-Pressure Vapor-Assisted Solution Process, *ACS Appl. Mater. Interfaces*, 2017, **9**, 2449–2458.

44 H. Shi, L. Zhang, H. Huang, X. Wang, Z. Li, D. Xuan, C. Wang, Y. Ou, C. Ni and D. Li, Simultaneous Interfacial Modification and Defect Passivation for Wide-Bandgap Semitransparent Perovskite Solar Cells with 14.4% Power Conversion Efficiency and 38% Average Visible Transmittance, *Small*, 2022, **18**, 2202144.

45 T. Zhang, M. Long, K. Yan, M. Qin, X. Lu, X. Zeng, C. M. Cheng, K. S. Wong, P. Liu and W. Xie, Crystallinity preservation and ion migration suppression through dual ion exchange strategy for stable mixed perovskite solar cells, *Adv. Energy Mater.*, 2017, **7**, 1700118.

46 Y. Zhou, M. Yang, S. Pang, K. Zhu and N. P. Padture, Exceptional morphology-preserving evolution of formamidinium lead triiodide perovskite thin films *via* organic-cation displacement, *J. Am. Chem. Soc.*, 2016, **138**, 5535–5538.

47 D. J. Kubicki, D. Prochowicz, A. Hofstetter, P. Pechy, S. M. Zakeeruddin, M. Gratzel and L. Emsley, Cation dynamics in mixed-cation $(MA)_x(FA)_{1-x}PbI_3$ hybrid perovskites from solid-state NMR, *J. Am. Chem. Soc.*, 2017, **139**, 10055–10061.

48 M. Mateen, H. Shi, H. Huang, Z. Li, W. Ahmad, M. Rafiq, U. A. Shah, S. Sajid, Y. Ren and J. Park, Graded 2D/3D Perovskite Hetero-Structured Films with Suppressed Interfacial Recombination for Efficient and Stable Solar Cells *via* DABr Treatment, *Molecules*, 2023, **28**, 1592.

49 M. Mateen, Z. Arain, X. Liu, A. Iqbal, Y. Ren, X. Zhang, C. Liu, Q. Chen, S. Ma and Y. Ding, Boosting optoelectronic performance of $MAPbI_3$ perovskite solar cells *via* ethylammonium chloride additive engineering, *Sci. China Mater.*, 2020, **63**, 2477–2486.

50 L. Li, Y. Chen, Z. Liu, Q. Chen, X. Wang and H. Zhou, The additive coordination effect on hybrids perovskite crystallization and high-performance solar cell, *Adv. Mater.*, 2016, **28**, 9862–9868.

51 W. Zhao, P. Guo, J. Su, Z. Fang, N. Jia, C. Liu, L. Ye, Q. Ye, J. Chang and H. Wang, Synchronous passivation of defects with low formation energies *via* terdentate anchoring enabling high performance perovskite solar cells with efficiency over 24%, *Adv. Funct. Mater.*, 2022, **32**, 2200534.

52 W. Peng, X. Miao, V. Adinolfi, E. Alarousu, O. El Tall, A. H. Emwas, C. Zhao, G. Walters, J. Liu and O. Ouellette, Engineering of $CH_3NH_3PbI_3$ perovskite crystals by alloying large organic cations for enhanced thermal stability and transport properties, *Angew. Chem., Int. Ed.*, 2016, **55**, 10686–10690.

53 Y. Doumbia, A. Bouich, B. M. Soucasse and D. Soro, Boosting the stability and growth of methylammonium lead bromide perovskites film doped with FA for solar cells, *Opt. Mater.*, 2023, **137**, 113563.

54 S. Wang, A. Wang and F. Hao, Toward stable lead halide perovskite solar cells: A knob on the A/X sites components, *iScience*, 2022, **25**, 103599.

55 C. Liu, Y. Yang, K. Rakstys, A. Mahata, M. Franckevicius, E. Mosconi, R. Skackauskaite, B. Ding, K. G. Brooks and O. J. Usiobo, Tuning structural isomers of phenylenediammonium to afford efficient and stable perovskite solar cells and modules, *Nat. Commun.*, 2021, **12**, 6394.